Nearly Quantum-Limited Josephson-Junction Frequency-Comb Synthesizer

Pinlei Lu, Tzu-Chiao Chien, Xi Cao, Olivia Lanes, Chao Zhou, Michael J. Hatridge, Saeed Khan, and Hakan E. Türeci

Nearly quantum-limited Josephson-junction Frequency Comb synthesizer

Pinlei Lu*, Tzu-Chiao Chien, Xi Cao, Olivia Lanes, Chao Zhou, and Michael J. Hatridge
Department of Physics and Astronomy, University of Pittsburgh
Saeed Khan*, Hakan E. Türeci
Department of Electrical Engineering, Princeton University
*These authors contributed equally to this publication.

(Dated: March 31, 2021)

While coherently-driven Kerr microcavities have rapidly matured as a platform for frequency comb formation, such microresonators generally possess weak Kerr coefficients; consequently, triggering comb generation requires millions of photons to be circulating inside the cavity. This suppresses the role of quantum fluctuations in the comb's dynamics. In this paper, we realize a minimal version of coherently-driven Kerr-mediated microwave frequency combs in the circuit QED architecture, where the quantum vacuum's fluctuations are the primary limitation on comb coherence. We achieve a comb phase coherence of up to 35 μs, approaching the theoretical device quantum limit of 55 μs, and vastly longer than the modes' inherent lifetimes of 13 ns. The ability within cQED to engineer stronger nonlinearities than optical microresonators, together with operation at cryogenic temperatures, and excellent agreement of comb dynamics with quantum theory indicates a promising platform for the study of .

While the circuit QED (cQED) architecture has built its success on strongly-coupled qubit-cavity experiments[1–5], it has also been firmly established as a versatile platform to realize a broader variety of quantum nonlinear systems[6]. Josephson-junction junction based superconducting circuits have also enabled devices from quantum-limited amplifiers[7–11] and single-microwave photon detectors[12–15] with application ranging from quantum information processing to the search for dark matter axions, to hybrid quantum systems[16]. A key factor determining the breadth of realizable quantum nonlinear devices, and thus feasibility of future applications, is understanding the diverse dynamical regimes enabled by Josephson-junctions.

A nonlinear dynamical regime that has yet to be realized via a Josephson-junction mediated Kerr nonlinearity is that of frequency comb formation. Distinct from Kerr-nonlinear amplifiers which operate in regimes with at least one classically stable fixed point in phase space, frequency comb formation is marked by a system undergoing stable periodic excursions around *unstable* fixed points. In the optical domain, coherently-driven microresonators utilizing the Kerr nonlinearity have emerged as the leading platform for frequency comb generation[17–22]; however the typically weak Kerr nonlinearity of optical microresonators[23] means that contemporary comb generation requires $\sim \mu$W power input[24], corresponding to millions of circulating cavity photons[25]. Similar results have been achieved in superconducting circuits using the weak nonlinearity of kinetic-inductance in very long resonators[26]. As a result, vacuum fluctuations amplified by the comb-generating nonlinear process are much weaker in comparison[27].

In this paper, we harness the Josephson junction to realize a minimal version of Kerr-mediated microwave frequency combs based on a recent theoretical proposal[28]. Our minimal realization within cQED consists of just two coupled modes, of which only one possesses a Kerr non-

linearity furnished by Josephson junctions, as shown in Fig. 1. Although our device is based on familiar cQED components, it operates in a distinct regime within the landscape of nonlinear cQED devices: while strongly-coupled like transmon-cavity systems[29], its nonlinearity is in fact weaker and is operated under much stronger driving. On the other hand, the device exhibits stronger couplings yet smaller detunings and weaker drives than Kerr-mediated bifurcation and parametric amplifiers[7,30]. This allows us to realize a ~~novel~~ unstable regime where a single frequency drive tone generates coherent frequency combs over a large parameter space.

Crucially, the strong engineerable nonlinearities in cQED and operation at cryogenic temperatures brings quantum fluctuations to the fore ahead of thermal and dephasing effects in our comb synthesizer: the phase coherence of the generated combs is fundamentally limited by vacuum fluctuations that are amplified by the nonlinear comb-generating process itself. A microscopic nonlinear quantum theory of our two-mode device, in addition to providing precise operating parameters for this comb-generating regime, enables us to quantify this quantum limit on comb phase coherence. By also characterizing and explaining the dependence of coherence on operating parameters like detuning and drive power, we provide a detailed quantitative study of the phase coherence of frequency combs near the quantum limit.

Built up of fundamentally quantum components, we believe this highly-controllable cQED realization can serve as a necessary building block for Kerr-nonlinear systems operating in classically-unstable *and* deeply-quantum regimes, exploring dynamics beyond coherent frequency comb formation. For certain parameter regimes, our device exhibits temporal instabilities marked by large, irregular excursions in phase space, distinct from regular comb dynamics and reminiscent of chaos. More excitingly, while our work indicates that strong quantum fluctuations limit the coherence of gen-
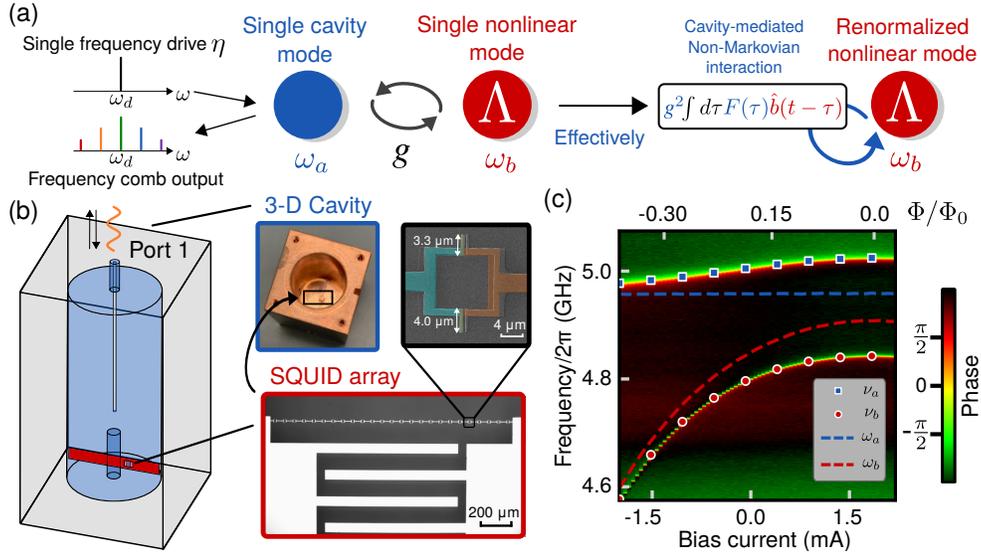
Figure 1. **System schematic and flux sweep.** (a) The two-mode device can be represented by a single cavity mode (blue, ω_a) coupled linearly to a single Kerr mode (red, ω_b). We create a comb in this device by driving with a carefully chosen, single microwave drive of strength η at frequency ω_d, which interacts with the device to create a series of tones at regularly spaced output frequencies (the 'comb'). The linear mode plays the role of mediating a delayed self-interaction of the nonlinear mode (right panel), with kernel $F(\tau) = e^{-\tau/\chi_a}$. In the strong coupling regime, the interaction's non-Markovian nature fundamentally modifies the nonlinear mode's stability, enabling comb formation. (b) Circuit QED implementation of the schematic in (a). The nonlinear mode inductance is formed by 25 Superconducting QUantum Interference Devices (SQUIDs) in series; False-color SEM image of a component SQUID indicates the small asymmetry employed to alleviate hysteresis. The SQUID array is coupled to an antenna that both forms the capacitance of the nonlinear mode and controls its dipole coupling with the linear mode; the latter is the $\lambda/4$ mode of a coaxial 3-D cavity, fabricated of copper to permit the passage of an external DC flux that threads all the SQUIDs. The input signal drives the cavity through port 1, and $S_{11}(\omega)$ is monitored. (c) Color plot of reflected signal vs. frequency from port 1 ($S_{11}(\omega)$) for a range of applied coil bias currents/applied SQUID fluxes. The linear and nonlinear mode frequencies are highlighted by blue squares and red dots respectively. By fitting for the bare mode frequencies, we determine $g/2\pi = 87.6956$ MHz, as well as the bare mode frequencies, represented by the dashed lines.

erated frequency combs, they are also features of deeply-quantum regimes necessary for displaying quantum effects such as squeezing, entanglement, and generation of non-Gaussian states. Our realization thus marks a promising first step in exploring the potentially competing role of strong quantum fluctuations in quantum dynamics within classically unstable regimes.

THEORY AND RESULTS

System schematic and device overview. The Hamiltonian of our device consists of a linear mode $\hat{a}$ with uncoupled resonant frequency ω_a, linearly coupled with strength g to a nonlinear mode $\hat{b}$ with uncoupled resonant frequency ω_b; see Fig. 1(a). The linear mode is driven by a coherent tone with frequency ω_d and amplitude η, and the system Hamiltonian in the frame rotating with this drive takes the form:

$$\hat{\mathcal{H}}/\hbar = -\Delta_{da}\hat{a}^\dagger\hat{a} - \Delta_{db}\hat{b}^\dagger\hat{b} - \frac{\Lambda}{2}\hat{b}^\dagger\hat{b}^\dagger\hat{b}\hat{b}$$
$$+ g(\hat{a}^\dagger\hat{b} + \hat{a}\hat{b}^\dagger) + \eta(\hat{a} + \hat{a}^\dagger) \quad (1)$$

where $\Delta_{da/db} = \omega_d - \omega_{a/b}$ and $\Lambda > 0$ is the strength of the Kerr nonlinearity. In our experiment (Fig. 1(c)), the nonlinear mode is realized as a Superconducting QUantum Interference Device (SQUID)[31] array (Device A: 25 SQUIDs; Device B: 5 SQUIDs). The SQUIDs act together as a flux-tunable, nonlinear inductor, which is shunted with a planar interdigitated capacitor/antenna to form a nonlinear microwave mode. Weakly asymmetric SQUIDs (with critical current ratio of 1.2:1) are used to build up the array, alleviating otherwise large hysteresis effects at the cost of a reduction in tunability of the nonlinear mode frequency[32]. The device is deposited on a sapphire substrate and capacitively coupled to the $\lambda/4$ mode of a coaxial 3-D copper cavity[33]. This driven-dissipative system is then described by the master equation: $\dot{\hat{\rho}} = -i[\hat{\mathcal{H}}, \hat{\rho}] + \kappa\mathcal{D}[\hat{a}]\hat{\rho} + \gamma\mathcal{D}[\hat{b}]\hat{\rho} + \gamma_\varphi\mathcal{D}[\hat{b}^\dagger\hat{b}]\hat{\rho}$, which includes linear damping rates κ (γ) for modes $\hat{a}$ ($\hat{b}$), and pure dephasing (γ_φ) for the flux-tunable nonlinear mode; thermal fluctuations are neglected. By sweeping the flux through the SQUIDs to tune the nonlinear mode frequency, and making a measurement of the reflection coefficient $S_{11}(\omega)$, we extract (Fig. 1(c)) a coupling strength of $g/2\pi = 87.6956$ MHz between the modes, and linear mode damping rate $\kappa/2\pi = 10.9308$ MHz.

Via pump-probe measurements[34] we also extract a Kerr nonlinearity of $\Lambda/2\pi = 5.96$ kHz, such that $\Lambda/\kappa \sim 10^{-3}$, stronger than typical values of $\sim 10^{-5}$ for optical microresonators[23,34].

Comb generation and phase diagram. Analysis of this system in Ref.[28] showed that the linear mode effectively equips the nonlinear mode with a delayed self-interaction (see Fig. 1(a)), whose influence is dictated by the coupling g and the linear mode susceptibility $\chi_a = (-i\Delta_{da} + \frac{\kappa}{2})^{-1}$. Under suitable coupling, drive, and detuning conditions, this two-mode system can go beyond typical bifurcation dynamics associated with Kerr nonlinear devices to exhibit frequency comb formation. To illustrate this, we plot the classical phase diagram for measured Device A parameters in Fig. 2(a), as a function of drive detunings Δ_{da}, Δ_{db}. For each pair of detunings, we consider a range of experimentally accessible drive powers (-132 dBm to -67 dBm), and classify phases according to the number of fixed points (FPs) and stable fixed points (SFPs) observable within this driving range. For large $|\Delta_{da}|$ (small $|\chi_a|$) relative to g, only two types of phases are exhibited: blank regions, where the system admits one SFP for all driving powers considered, or hatched regions, where for some subset of driving powers, three FPs exist. In either case, at least one fixed point is always stable[28]. These phases are reminiscent of the standard Kerr bistability, and unsurprisingly so: in this regime, the effective coupling $g|\chi_a|$ is weak, and the mediated interaction may be treated within a Markov approximation.

However, for intermediate $|\Delta_{da}|$ such that $g|\chi_a| \gtrsim 1$ (on resonance, we require $g > \kappa/2$, comfortably satisfied by Device A), the non-Markovian nature of the interaction manifests in a qualitative change of the nonlinear mode's stability, marked by regions (shaded red) where no stable fixed points exist for a subset of the driving powers considered. Here, classical Lyapunov analysis reveals the possibility of our device exhibiting stable limit cycles with period $T = \frac{2\pi}{\Delta}$ and comb-like frequency spectra with spacing Δ, and even chaotic dynamics deeper into the unstable regime.

To observe the response of our quantum device in this rich dynamical regime, we enter the unstable region along the green arrow in Fig. 2 (a), by fixing the drive frequency so that $\Delta_{da}/2\pi = -47.8$ MHz, and flux tuning the nonlinear mode frequency. In search of the frequency domain signature of comb formation, we measure the

Figure 2. **Phase diagram and comb spectrum**. (a) Theoretically predicted phase diagram in Δ_{db}-Δ_{da} space, indicating observable phases characterized by number and stability of classical fixed points (FPs) over a range of experimentally accessible drive powers (-132 dBm to -67 dBm, see text for details). Here, the unstable regime (shaded red) exhibiting no stable fixed points (SFPs) is entered by fixing the drive frequency to $\omega_d = 4.9085(2\pi)$ GHz, varying the nonlinear mode frequency along the direction of the green arrow via a flux sweep (see schematic), and observing the output power spectra. (b) Typical power spectra as a function of increasing drive power, along the indicated cross section of the experimental phase diagram in (c). At low powers, the system exhibits single frequency output at ω_d (1), marked gray in the phase diagram. With increasing drive power (2), the system enters a regime with regularly spaced multifrequency output, with spacing Δ which is plotted in the phase diagram in Drive-Δ_{db} space. With stronger driving power (3), the spacing Δ increases, while fewer side peaks are observed above the noise background, before the system ultimately exits the unstable regime and single frequency output resumes. The theoretical phase diagram is plotted in the top panel of (c) for comparison.

frequency response in drive-Δ_{db} parameter space using a spectrum analyzer, with typical results at fixed Δ_{db} shown in Fig. 2(b). At low powers (1), the system exhibits a single frequency response at the drive frequency, corresponding to the stable fixed point. However, as the power is increased, a multifrequency spectrum emerges with equidistant peaks (2 and 3). The spacings Δ extracted from these power spectra are used to construct the experimental phase diagram in Fig. 2(c), with the theoretical result over the same parameter space provided for comparison. We find remarkable agreement between theory and experiment; only a single fitting offset is used to account for scaling factors along the drive power axis.

Temporal coherence and dynamical response.

	Device A (25 SQUIDs)	Device B (5 SQUIDs)
$\omega_b/2\pi$(GHz)	4.956806	4.951073
$g/2\pi$(MHz)	87.6956	89.25
$\Lambda/2\pi$(MHz)	5.96×10^{-3}	152.6×10^{-3}
$\kappa/2\pi$(MHz)	10.9308	22.84

Table I. **Device parameters.** Coupling strength g, nonlinearity Λ, and bare cavity damping rate κ for Device A (25 SQUIDs) and Device B (5 SQUIDs); nonlinearity suppression by a factor ~ 25 is measured, as designed.
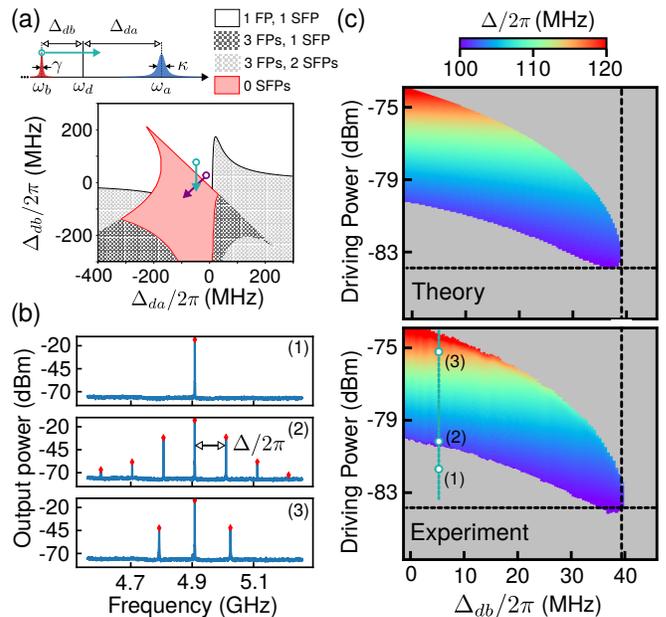
Power spectrum measurements provide a key signature of comb formation but are insensitive to the nontrivial phase dynamics of these complex nonlinear solutions. While the central comb peak has a definite phase set by the incident coherent tone, the relative phase $\theta(t)$ of generated sidebands relative to the central peak phase is free to diffuse[35,36]. This diffusion sets the comb linewidth and thus provides the ultimate limit to any precision measurements made using the comb in question[37]. To quantify the phase coherence, we measure the *steady-state* first-order temporal coherence function $G^{(1)}(\tau)$, defined as[38]:

$$G^{(1)}(\tau) = \lim_{t \to \infty} \frac{\langle I(t)I(t+\tau)\rangle - \langle I(t)\rangle^2}{\langle I(t)^2\rangle - \langle I(t)\rangle^2} \qquad (2)$$

To do so, we first obtain the time-domain cavity output $I(t)$ using a single side band (SSB) mixer to downconvert the dominant sideband peak to around the 100 MHz regime, followed by homodyne detection via a 500 MSample/s digitizer to demodulate the output signal, and finally compute its time-domain autocorrelation. The normalized coherence function $G^{(1)}(\tau)$ decays from its maximum value of unity (at $\tau = 0$) towards $G^{(1)}(\tau) = 0$ over a time scale T_{coh} determined by the loss mechanisms affecting the system dynamics. We measure $G^{(1)}(\tau)$ in the parameter space explored in Fig. 2(c), and extract T_{coh} as the decay constant of the observed function envelopes; the results are plotted in Fig. 3(a). Focusing in particular on the indicated cross-section at $\Delta_{db}/2\pi = 25.2$ MHz, we plot the measured $G^{(1)}(\tau)$ functions at positions $\{1, 2, 3\}$ in the top panel of Fig. 3(c). Outside the comb regime (1), $G^{(1)}(\tau)$ decays on a timescale of ~ 13 ns, set by the fastest decay rate, namely the bare cavity loss κ. However, a qualitative change is observed in $G^{(1)}(\tau)$ when the system transitions into the comb regime (2), with a sharp increase in coherence time to a maximum of 36.7 μs, significantly longer than the timescale set by κ. This observation, together with the decrease in T_{coh} with increasing drive power (3), highlights a key feature of the self-oscillating regime: the intrinsic energy loss of the system is overcome and coherence is therefore no longer determined by the bare energy loss rates.

This naturally raises the question: what limits the observed phase coherence? The answer lies in the full quantum description of the strongly-driven, weakly nonlinear two-mode system. In this regime, we employ a phase-space approach based on the Positive-P representation[28,39,40], obtaining a set of stochastic differential equations (SDEs) for phase space variables $\vec{\zeta} = (\alpha, \alpha^{\dagger}, \beta, \beta^{\dagger})^T$ associated with operators $(\hat{a}, \hat{a}^{\dagger}, \hat{b}, \hat{b}^{\dagger})^T$. The SDEs take the general form :

$$d\vec{\zeta}(t) = \vec{A}_{\text{c}}(\vec{\zeta})\, dt + \mathbf{B}_{\text{st}}(\vec{\zeta}, \Lambda, \gamma_{\varphi})d\vec{W}(t) \qquad (3)$$

The deterministic contribution ($\propto \vec{A}_{\text{c}}$) describes noise-free classical dynamics of the two-mode system, which yields perfectly coherent combs. The remaining stochastic terms $\propto d\vec{W}(t)$ (vector of independent Wiener increments) then describe deviations from classical dynamics, here including fluctuations due to the quantum nonlinearity Λ and pure dephasing γ_{φ}. These fluctuations are ultimately responsible for phase diffusion that limits comb coherence. The stochastic terms take the explicit form $\mathbf{B}_{\text{st}}(\vec{\zeta}, \Lambda, \gamma_{\varphi})d\vec{W}(t) = \sqrt{\Gamma}\mathbf{B}_1(\vec{\zeta})d\vec{W}_1(t) + \sqrt{\gamma_{\varphi}}\mathbf{B}_2(\vec{\zeta})d\vec{W}_2(t)$, where $\Gamma = \sqrt{\Lambda^2 + \gamma_{\varphi}^2}$. Crucially, we note that even in the absence of pure dephasing, $\gamma_{\varphi} \to 0$, the stochastic terms do not vanish: a contribution due to the intrinsic nonlinearity of the system always remains, setting a fundamental limit on comb coherence. This is verified by simulating Eqs. (3) for $\gamma_{\varphi} = 0$ and the experimentally measured nonlinearity of $\Lambda/2\pi = 5.96$ kHz, and obtaining T_{coh}[41,42]; the results are shown by the blue curve in Fig. 3(b), with the blue shaded region being a 95% confidence bound accounting for uncertainty in Λ. The maximum T_{coh} is thus limited to around 55 μs by amplified quantum fluctuations due to the device nonlinearity alone under these operating conditions. This of course exceeds the maximum observed T_{coh} since $\gamma_{\varphi} \neq 0$. For $\gamma_{\varphi}/2\pi \simeq 2.0$ kHz (orange) we find good agreement with experiment (gray) ; simulated $G^{(1)}(\tau)$ at positions $\{1, 2, 3\}$ are shown (Fig. 3 c, black) for comparison. The relatively small γ_{φ} is not unexpected given both the narrow modulation range of the asymmetric SQUID array[32] and operation at $\Phi/\Phi_0 \lesssim 0.12$, close to the flux noise sweet spot (see Fig. 1).

Since Λ cannot be varied *in-situ* while holding other parameters fixed, we confirm its influence on T_{coh} by employing Device B; this 5-SQUID device is engineered to have the same total inductance as Device A, while possessing a 25-fold stronger nonlinearity[43] of $\Lambda/2\pi = 152.6$ kHz. While we obtain similar multifrequency behaviour (full results in SI[34]), coherence times for this device are much shorter, $T_{\text{coh}} \lesssim 1.5$ μs (see Fig. 3(c) for measured and simulated $G^{(1)}(\tau)$ at typical operating parameters). Although Device B is operated away from the flux-noise sweet spot[34], and thus experiences a larger estimated $\gamma_{\varphi}/2\pi \simeq 30.0$ kHz, we find that its much stronger nonlinearity is dominant in limiting comb coherence. To confirm the dependence of T_{coh} on Λ and γ_{φ} numerically, we simulate T_{coh} at fixed positions on the phase diagrams of both devices, while varying Λ. The results are plotted in Fig. 3(d), in purple (green) for Device A (Device B) parameters, with the experimental result indicated by the square (diamond). They are well described by fits to $T_{\text{coh}} = a(\gamma_{\varphi} + b\Lambda)^{-1}$ (curves); we find $b = (\text{A}: 0.40, \text{B}: 0.55) \neq 1$, consistent with Λ and γ_{φ}-contributions to dephasing originating from different stochastic terms in Eqs. (3). More importantly, both devices clearly operate in the regime where $b\Lambda \gtrsim \gamma_{\varphi}$, and thus T_{coh} is predominantly set by the nonlinearity.

However, as observed in Fig. 3(a), T_{coh} also depends nontrivially on *operating* parameters (e.g. drive power, detuning), even if Λ, γ_{φ} are held fixed. This dependence is intimately related to the nature of the dynamical comb regime, where the system traverses a periodic

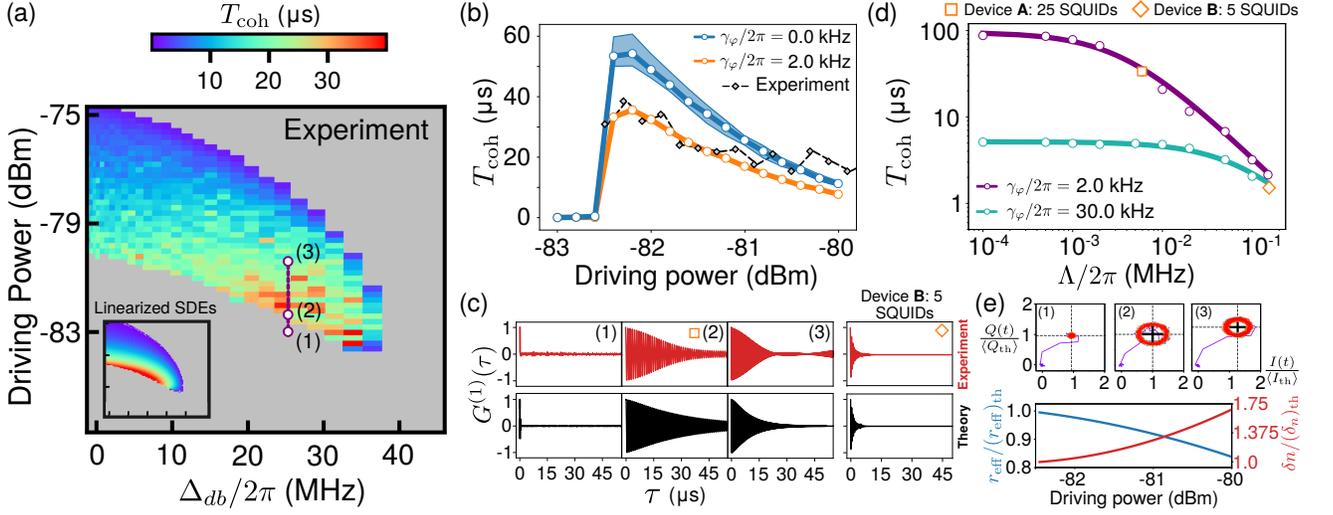Figure 3. **Comb coherence.** (a) Coherence time T_{coh} extracted by measuring $G^{(1)}(\tau)$ (Eq. 2) for the same operating parameters as Fig. 2 b. Inset: approximate T_{coh} calculated using Floquet analysis of linearized SDEs (see text). (b) Cross section of phase diagram along the dashed line in a, in black. The blue curve and shaded region indicates the theoretically calculated coherence time due to nonlinearity alone (pure dephasing $\gamma_\varphi = 0$). The orange curve shows T_{coh} for $\gamma_\phi = 2.0(2\pi)$ kHz, showing good agreement with the experimental result. (c) Experimental (top panel) and theoretical (lower panel) $G^{(1)}(\tau)$ for $\gamma_\varphi = 2.0(2\pi)$ kHz at positions 1 (stable regime), 2 (threshold of comb formation), and 3 (higher drive power in comb regime). (d) Numerical results for variation of coherence time with nonlinearity. Purple and green points correspond to parameters for Device A (25 SQUIDs) and B (5 SQUIDs) respectively, obtained by varying the nonlinearity alone. Experimental results for the devices are shown by the orange square and diamond; corresponding $G^{(1)}(\tau)$ are marked by the same symbols in (c). Curves are fits to $T_{\mathrm{coh}} = a(\gamma_\varphi + b\Lambda)^{-1}$, with $(a,b) = (1.19, 0.55)$ for Device A and $(0.94, 0.40)$ for Device B. (e) Top panel: I-Q trace at positions $\{1,2,3\}$, showing 2-D projection of the limit cycle orbit which decreases in radius with increasing power. Lower panel: theoretical effective radius of limit cycle r_{eff} (solid blue) and standard deviation of noise projected tangential to limit cycle, δn (solid red, right hand axis). The decrease in r_{eff} combined with the increase in δn point towards a reduction in coherence time with increasing drive power (see text).

trajectory in phase space. The shape of this trajectory, which changes with operating parameters, controls its susceptibility to noise, as well as the noise itself when the latter is *multiplicative* (dependent on $\vec\zeta(t)$, as $\mathbf{B}_{\mathrm{st}}$ is). This connection can be made precise via a linearized Floquet analysis[36,44,45] of the SDEs around the *classical* limit cycle trajectory $\vec\zeta_c(t)$. In this weak-fluctuations approach[34,46], the phase $\theta(t)$ of the limit cycle solution evolves according to the SDE: $r_{\mathrm{eff}}\dot\theta = n(t)$, and the coherence time T_{coh} can be related to the variance of this diffusing phase, . Here r_{eff} is the effective limit cycle radius, defined via $r_{\mathrm{eff}}\Delta = \sqrt{\frac{1}{T}\int_0^T dt\, ||\vec v(t)||^2}$ where $\vec v(t) = \dot{\vec\zeta}_c(t)$ is the tangential velocity of limit cycle traversal. Secondly, $n(t)$ is the projection of stochastic terms $\mathbf{B}_{\mathrm{st}}(\vec\zeta_c(t))d\vec W$ onto the limit cycle trajectory. Noise projected onto the limit cycle therefore provides an impulse that causes $\theta(t)$ to diffuse, while r_{eff} provides an inertial term: the larger the radius, the more $\theta(t)$ resists diffusion. We plot the average projected noise standard deviation, $\delta n = \sqrt{\frac{1}{T}\int_0^T dt\, \langle n(t)^2\rangle}$ and the effective limit cycle radius r_{eff} along the indicated cross-section of Fig. 3(a), scaled by their values at the threshold of comb formation. The limit cycle radius (blue) decreases with in-

creasing power; this is also seen experimentally in I-Q traces (top panel), positions 2 to 3, which can be viewed as a 2-D Poincaré section of the limit cycle trajectory. Additionally, the noise strength δn (red, right hand axis) increases, in a clear manifestation of its multiplicative nature. Both effects tend to reduce T_{coh}, as captured by both the linearized analysis (Fig. 3(a), inset) and full SDE simulations (Fig. 3(b)).

Temporal instabilities and further explorations. While we have demonstrated the formation of stable frequency combs with this minimal two-mode Kerr system, even more complex dynamical phenomena may be observed deeper in the regime with no stable fixed points. We explore this region by fixing $\omega_b = 4.91$ GHz and varying ω_d instead, now entering the unstable region along the purple arrow in Fig. 2(a). The experimental phase diagram in Fig. 4(a) plots spacings Δ where combs are observed, together with a dark gray region where the spectrum no longer exhibits a comb. The typical variation in spectrum is shown in Fig. 4(b). For $\Delta_{db}/2\pi \gtrsim -30$ MHz, a clear comb spectrum is observed with a spacing that varies with ω_d; the system polariton frequencies ν_a, ν_b (unchanged with ω_d) are marked in dashed pink, confirming that comb peaks do not always coincide with passive modes of the two-mode system.
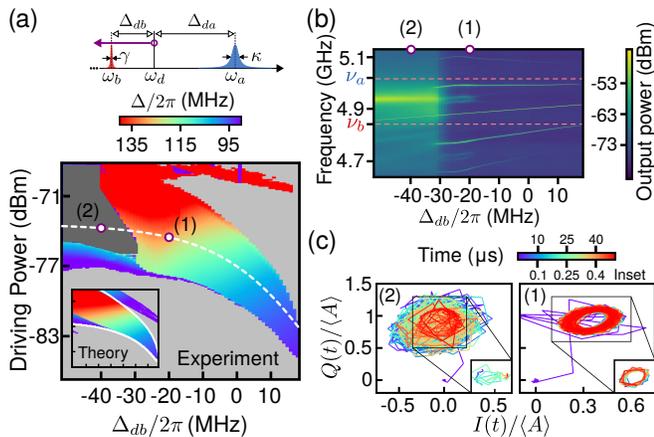
Figure 4. **Temporal instabilities.** (a) By fixing ω_a, ω_b and varying ω_d (top panel), the system can be driven to the regime with no stable fixed points along the purple arrow in Fig. 2 (a), while leaving the underlying mode structure unchanged. The resulting phase diagram plotting observed comb spacing Δ is shown, with the theoretical prediction in the inset. For $\Delta_{db}/2\pi \lesssim -30$ MHz and strong enough driving, a distinct regime emerges (dark gray) where the output spectrum broadens significantly. In (b), we show the typical evolution of the spectrum across the white dashed line, chosen to show a large variation in comb spacing. In dashed red are the underlying polariton resonances, indicating that the emergent comb peaks do not exactly coincide with these resonances. (c) Time dynamics as observed via I-Q traces, with both axes scaled by $\langle A \rangle = \sqrt{\langle I^2 \rangle + \langle Q^2 \rangle}$ at position 1, for ease of direct comparison. In the stable comb regime (1), the cavity response settles into an obvious orbit as before; the inset shows a 500 ns trace after $t = 40$ μs, demonstrating the stable orbit. In the unstable regime (2), the response shows large deviations over time and no periodic phase space trajectory is observed.

For $\Delta_{db}/2\pi \lesssim -30$ MHz, the spectrum abruptly changes, exhibiting a single broad peak and an increased noise background. Analyzing I-Q traces in Fig. 4(c), dynamics in this region (2) show large deviations with time and while recurringly confined to a region of phase space do not follow a regular trajectory, even on short timescales (inset), in stark contrast to regular periodic dynamics for stable comb operation (1). Note that these temporal instabilities disagree with results of a weak quantum fluctuations analysis in this regime (Fig. 4(a), inset), which simply predicts frequency combs with finite coherence akin to Fig. 3 (although instabilities do manifest for more negative detunings[34]). Curiously, quantum dynamics here are also too complex to be captured by simulating the exact SDEs in Eqs. (3), which run into familiar numerical difficulties encountered in the application of phase-space stochastic approaches to strong-quantum systems[50]. This could be indicative of qualitative deviations from classically stable limit cycles not captured by a linearized treatment of quantum fluctuations, and merits further study of this system as a platform for .

DISCUSSION AND OUTLOOK

We have realized a minimal two-mode Kerr system for generating coherent frequency combs under excitation by a single coherent tone. The phase coherence of the generated combs is fundamentally limited by the intrinsic nonlinearity strength in the quantum modes which form the device. The excellent agreement between theory and experiment points toward a highly controllable experimental platform for the study of complex nonlinear dynamics in the quantum regime. Our device realizes a classically-unstable Kerr-nonlinear regime, ideally suited to understand the potentially competing role of strong quantum fluctuations as a source of decoherence and non-classicality in moderate to strongly nonlinear quantum devices.

Finally, the versatility of the cQED platform admits extensions of our device to multimode systems, and to realizations employing tunable parametric couplers[51], paving the way towards an *in-situ* engineerable multi-frequency light source. Such frequency combs could enable multiplexed quantum measurement[52] using a single monochromatic incident tone. The generated combs could also function as multifrequency pumps to phase-coherently drive multiple parametric processes simultaneously in a single device for Hamiltonian engineering applications[53–56]. This could include the intriguing possibility of multifrequency pumps exhibiting non-classical coherences, using comb generators operating in the deep-quantum regime.

Appendix A: Stochastic description of quantum dynamics via the Positive-P representation

The derivation of the system Hamiltonian and master equation we consider in this paper is quite standard in cQED; in particular, it may be found in detail in the SI of our previous work[28], and we thus do not repeat the

derivation here. Instead, in this appendix section we begin with the master equation description, derive its corresponding classical description making use of a positive-P phase-space description, and analyze the stability of the resulting system.

For convenience, we reproduce here the master equation describing the dynamics of the two-mode system:

$$\dot{\rho} = -i[\hat{\mathcal{H}}, \hat{\rho}] + \kappa\mathcal{D}[\hat{a}]\hat{\rho} + \gamma\mathcal{D}[\hat{b}]\hat{\rho} + \gamma_\varphi\mathcal{D}[\hat{b}^\dagger\hat{b}]\hat{\rho} \quad (A1)$$

where the system Hamiltonian in the frame rotating with the drive is given by Eq. (1) from the main text.

In the weakly nonlinear regime relevant to the experiment, $\Lambda/\kappa \sim O(10^{-2}) - O(10^{-3})$, strong driving leads to large mode occupations $\sim O(10^2) - O(10^3)$, rendering standard master equation and even stochastic wavefunction approaches intractable for direct simulation. Such operating regimes are particularly suited to analysis using a phase-space approach to the dynamics of the density operator $\hat{\rho}$. In this appendix section, we describe the approach used in this work, that of the Positive-P representation of the density operator, and the resulting stochastic differential equations (SDEs) it yields. In Section III of the SI, we also describe how the SDEs may be solved numerically to obtain quantities of interest.

We employ a representation of the density operator in a non-diagonal coherent state basis over both modes $\hat{a}$ and $\hat{b}$:

$$\hat{\rho}(t) = \int d^2\zeta \; P(\vec{\zeta}, t) \; \hat{\Xi}_\alpha \otimes \hat{\Xi}_\beta$$

$$\equiv \int d^2\zeta \; P(\vec{\zeta}, t) \cdot \frac{|\alpha\rangle\langle\alpha^{\dagger*}|}{e^{\alpha\alpha^\dagger}} \otimes \frac{|\beta\rangle\langle\beta^{\dagger*}|}{e^{\beta\beta^\dagger}} \quad (A2)$$

where $\vec{\zeta} = (\alpha, \alpha^\dagger, \beta, \beta^\dagger)$ are complex variables describing a classical phase space, $\vec{\zeta} \in \mathbb{C}^4$. For convenience of notation, we use ζ_i to refer to the ith element of the vector $\vec{\zeta}$, for $i = 1, \ldots 4$, and define $d^2\zeta \equiv \prod_i d^2\zeta_i$ as the integration measure over the entire phase space.

Eq. (A2) is simply an expansion of $\hat{\rho}(t)$ in terms of non-diagonal projection operators $\hat{\Xi}_\alpha \otimes \hat{\Xi}_\beta$, with weights given by the time-dependent function $P(\vec{\zeta}, t)$. For the above definition of $\hat{\Xi}_\alpha \otimes \hat{\Xi}_\beta$, $P(\vec{\zeta}, t)$ is positive-definite function that satisfies a Fokker-Planck equation, and therefore may be meaningfully thought of as a classical distribution function; in particular, $P(\vec{\zeta}, t)$ is referred to as the Positive-P distribution[39,40].

The above expansion casts the study of the dynamics of $\hat{\rho}(t)$ and operator averages $\langle\hat{o}\rangle = \text{tr}\{\hat{o}\hat{\rho}(t)\}$ into an equivalent study of the dynamics of the distribution function $P(\vec{\zeta}, t)$ and of probabilistic variables sampled from this distribution function. Phase space approaches therefore first require obtaining the dynamical equation for the distribution function $P(\vec{\zeta}, t)$, which takes the form of a nonlinear Fokker-Planck equation:

$$\partial_t P(\vec{\zeta}, t) = \left(-\partial_i A_c^i + \frac{1}{2}\partial_i\partial_j D_{st}^{ij}\right) P(\vec{\zeta}, t) \quad (A3)$$

where $\partial_i \equiv \frac{\partial}{\partial\zeta_i}$ and repeated indices are summed over. Here A_{cl}^i is the ith element of the drift vector $\vec{A}_{cl}$ that defines deterministic nonlinear dynamics:

$$\vec{A}_c = \begin{pmatrix} \left(+i\Delta_{da} - \frac{\kappa}{2}\right)\alpha - ig\beta - i\eta \\ \left(-i\Delta_{da} - \frac{\kappa}{2}\right)\alpha^\dagger + ig\beta^\dagger + i\eta \\ \left(+i\Delta_{db} - \frac{\gamma+\gamma_\varphi}{2}\right)\beta + i\Lambda(\beta^\dagger\beta)\beta - ig\alpha \\ \left(-i\Delta_{db} - \frac{\gamma+\gamma_\varphi}{2}\right)\beta^\dagger - i\Lambda(\beta^\dagger\beta)\beta + ig\alpha^\dagger \end{pmatrix} \quad (A4)$$

On the other hand, D_{st}^{ij} is the (i,j)th element of the diffusion matrix $\mathbf{D}_{st}$ that lends 'width' to the distribution function. Here it takes the simple form:

$$\mathbf{D}_{st} = \begin{pmatrix} \mathbf{0} & \mathbf{0} \\ \mathbf{0} & \mathbf{D}_\beta \end{pmatrix}, \mathbf{D}_\beta = \begin{pmatrix} (i\Lambda - \gamma_\varphi)\beta^2 & \gamma_\varphi\beta^\dagger\beta \\ \gamma_\varphi\beta^\dagger\beta & (-i\Lambda - \gamma_\varphi)(\beta^\dagger)^2 \end{pmatrix} \quad (A5)$$

where $\mathbf{0}$ is the 2-by-2 matrix of zeros. Note that the diffusion includes contributions arising from the nonlinearity Λ as well as from the the dephasing term γ_φ.

In general, the multi-dimensional nonlinear Fokker-Planck equation, Eq. (A3), cannot be analytically solved for the distribution function $P(\vec{\zeta}, t)$; exceptions include situations where the Fokker-Planck equation is linear or where certain potential conditions are satisfied[57]. The current system falls under neither category. However, the utility of the Fokker-Planck equation extends beyond the equation itself; one can also obtain a set of equivalent stochastic differential equations (SDEs) describing the dynamics of phase space variables $\vec{\zeta}(t)$ sampled from the Positive-P distribution satisfying the governing Fokker-Planck equation. The set of SDEs takes the form[39]:

$$d\vec{\zeta} = \vec{A}_c(\vec{\zeta})dt + \sqrt{\Gamma}\mathbf{B}_1(\vec{\zeta})d\vec{W}_1(t) + \sqrt{\gamma_\varphi}\mathbf{B}_2(\vec{\zeta})d\vec{W}_2(t) \quad (A6)$$

where $d\vec{W}_i$ are vectors of real, independent Wiener increments. The noise matrices $\mathbf{B}_1$, $\mathbf{B}_2$ are related to the square root of the diffusion matrix, $\mathbf{D}_{st} = \mathbf{B}_{st}\mathbf{B}_{st}^T$, where $\mathbf{B}_{st} = \sqrt{\Gamma}\mathbf{B}_1 + \sqrt{\gamma_\varphi}\mathbf{B}_2$. They can be written compactly in block form:

$$\mathbf{B}_1 = \begin{pmatrix} \mathbf{0} & \mathbf{0} \\ \mathbf{b}_1 & \mathbf{0} \end{pmatrix}, \; \mathbf{B}_2 = \begin{pmatrix} \mathbf{0} & \mathbf{0} \\ \mathbf{0} & \mathbf{b}_2 \end{pmatrix} \quad (A7)$$

where the 2-by-2 component matrices $\mathbf{b}_1$ and $\mathbf{b}_2$ are given by:

$$\mathbf{b}_1 = \begin{pmatrix} e^{i\theta/2}\beta & 0 \\ 0 & e^{-i\theta/2}\beta^\dagger \end{pmatrix}, \; \mathbf{b}_2 = \sqrt{\frac{\beta^\dagger\beta}{2}} \begin{pmatrix} e^{i\pi/4} & e^{-i\pi/4} \\ e^{-i\pi/4} & e^{i\pi/4} \end{pmatrix} \quad (A8)$$

Finally, we have defined the parameters Γ and θ via:

$$\Gamma e^{i\theta} \equiv i\Lambda - \gamma_\varphi \implies \Gamma = \sqrt{\Lambda^2 + \gamma_\varphi^2}, \; \theta = \arctan\left(-\frac{\Lambda}{\gamma_\varphi}\right) \quad (A9)$$

Eqs. (A6) are the same as Eq. (3) from the main text, and are the central equations we employ to analyze the dynamics of the two-mode system.

Appendix B: Classical limit, fixed points, and linear stability

While Eqs. (A6) describe the quantum dynamics of the two-mode system, they also allow us to analyze a well-defined classical limit, where the stochastic terms in Eqs. (A6) vanish. Clearly, the dephasing contribution $\propto \sqrt{\gamma_\varphi}\mathbf{B}_2$ can be dropped by setting $\gamma_\varphi = 0$. However, simply setting taking $\Lambda = 0$ will render the two-mode system linear and eliminate the comb dynamics we are interested in.

Instead, a simple scaling argument allows us to understand the classical limit of the two-mode system. We consider reducing the nonlinearity by a factor $\Lambda \to \Lambda/k$ ($k > 1$), and simultaneously transforming $\vec{\zeta} \to \sqrt{k}\vec{\zeta}$, $\eta \to \sqrt{k}\eta$. Under this transformation, we find that Eqs. (A6) become ($\gamma_\varphi = 0$):

$$d\vec{\zeta} = \vec{A}_c(\vec{\zeta})dt + \frac{1}{\sqrt{k}}\sqrt{\Lambda}\mathbf{B}_1(\vec{\zeta})d\vec{W}_1(t) \tag{B1}$$

More precisely, the drift vector $\vec{A}_c(\vec{\zeta})$ is *invariant* under this transformation, while the stochastic terms are scaled by a factor of $1/\sqrt{k}$. Physically, this transformation indicates that as the strength of the nonlinearity decreases, the deterministic dynamics remain unchanged provided the drive is suitably increased, upto a scaling of the mode amplitudes $\vec{\zeta}$. The stochastic dynamics, on the other hand, are suppressed. The appropriate classical limit that retains nonlinear dynamics can thus be realized by considering weak nonlinearities under sufficiently strong driving. The dynamical equations that describe this classical limit are thus given by:

$$d\vec{\zeta} = \vec{A}_c(\vec{\zeta})dt \quad \text{(classical limit, } k \to \infty) \tag{B2}$$

Upon dropping the stochastic terms, it is clear to see from the now *ordinary* differential equations above (when written out) that $\alpha^\dagger = \alpha^*$, $\beta^\dagger = \beta^*$; as a result, the deterministic dynamics in the classical limit, Eqs. (B2), can finally be written down entirely in terms of α, β:

$$\dot{\alpha} = \left(i\Delta_{da} - \frac{\kappa}{2}\right)\alpha - ig\beta - i\eta \tag{B3a}$$

$$\dot{\beta} = \left(i\Delta_{db} - \frac{\gamma}{2}\right)\beta + i\Lambda|\beta|^2\beta - ig\alpha \tag{B3b}$$

For completeness, we note here that the above system is the same as that obtained by writing down the equations of motion for operator averages $\{\langle\hat{a}\rangle, \langle\hat{b}\rangle\}$, neglecting correlations (namely performing replacements of the form $\langle\hat{b}^\dagger\hat{b}\hat{b}\rangle \to \langle\hat{b}^\dagger\rangle\langle\hat{b}\rangle\langle\hat{b}\rangle$), and finally replacing operator expectation values by complex amplitudes, $\{\langle\hat{a}\rangle, \langle\hat{b}\rangle\} \to \{\alpha, \beta\}$; the derivation here provides some context to the approximations underlying this dropping of correlations.

The linearity of both mode $\hat{a}$ and the coupling $\propto g$ enables the linear mode to be integrated out, leading to a single effective dynamical equation for the nonlinear mode amplitude[28]:

$$\dot{\beta} = \left(i\Delta_{db} - \frac{\gamma}{2}\right)\beta + i\Lambda|\beta|^2\beta - ig\chi_a\eta$$
$$- g^2\int_0^t d\tau\ F(\tau)\beta(t-\tau) \tag{B4}$$

where we have introduced the linear mode susceptibility $\chi_a = (-i\Delta_{da} + \frac{\kappa}{2})^{-1}$, and where the memory kernel for the self-interaction is given by:

$$F(\tau) = e^{(i\Delta_{da} - \kappa/2)\tau} \tag{B5}$$

The classical steady-state of the two-mode system $(\bar{\alpha}, \bar{\beta})$ may be obtained by setting $\dot{\bar{\beta}} = 0$ in Eq. (B4). This requirement simplifies the self-interaction term and is exactly equivalent to performing a Markov regime reduction of the same. The result is a cubic polynomial in $|\bar{\beta}|^2$ that can be solved exactly for the steady-state nonlinear mode amplitude $\bar{\beta}$:

$$\left[\left(\widetilde{\Delta}_{db} + \Lambda|\bar{\beta}|^2\right)^2 + \frac{\widetilde{\gamma}^2}{4}\right]|\bar{\beta}|^2 = g^2|\chi_a|^2\eta^2 \tag{B6}$$

where we have introduced the renormalized nonlinear mode detuning and damping parameters respectively:

$$\widetilde{\Delta}_{db} = \omega_d - (\omega_b + g^2|\chi_a|^2\Delta_{da})$$
$$\widetilde{\gamma} = \gamma + g^2|\chi_a|^2\kappa \tag{B7}$$

The steady-state linear mode amplitude may then be determined by requiring $\dot{\bar{\alpha}} = 0$ in Eq. (B3a), which simply relates $\bar{\alpha}$ to $\bar{\beta}$:

$$\bar{\alpha} = -\chi_a\left(ig\bar{\beta} + i\eta\right) \tag{B8}$$

Once the steady-state amplitudes $(\bar{\alpha}, \bar{\beta})$ have been determined, we perform a stability analysis for small fluctuations around these steady-state(s). Formally, such an analysis can be performed on the linearized version of the effective nonlinear mode dynamical equation, which can be studied analytically *exactly* in the Laplace domain, and is particularly tractable for the special case where $\Delta_{da} = 0$. Full details of such an analysis are provided in Ref.[28].

However, the current experiment explores more general operating conditions where $\Delta_{da} \neq 0$ in general. In this case, it proves most convenient to simply perform a numerical stability analysis based on the Jacobian matrix of the original two-mode system. Performing the linearized stability analysis requires expanding Eqs. (B2) around the classical steady state $(\bar{\alpha}, \bar{\beta})$. For notational convenience, we define the vector of steady-state amplitudes $\vec{Z}$ and small fluctuations $\vec{z}(t)$ respectively:

$$\vec{Z} = (\bar{\alpha}, \bar{\alpha}^*, \bar{\beta}, \bar{\beta}^*)^T \tag{B9a}$$

$$\vec{z}(t) = (\delta\alpha(t), \delta\alpha^*(t), \delta\beta(t), \delta\beta^*(t))^T \tag{B9b}$$

Then, we expand the variables $\vec{\zeta}(t)$ around the steady-state $\vec{Z}$:

$$\vec{\zeta}(t) = \vec{Z} + \vec{z}(t) \tag{B10}$$

and linearize Eqs. (B2) in small fluctuations $\vec{z}(t)$, obtaining the set of equations:

$$\frac{d\vec{z}}{dt} = \mathbf{J}[\vec{Z}] \cdot \vec{z}(t) \tag{B11}$$

where $\mathbf{J}[\vec{Z}]$ defines the Jacobian matrix of the two-mode system evaluated at the classical steady-state; its entries are given by $J_{ij} = \partial_j A_c^i$, where A_c^i is the ith element of $\vec{A}_c$; more explicitly the Jacobian matrix takes the form:

$$\mathbf{J}[\vec{Z}] = \begin{pmatrix} +i\Delta_{da} - \frac{\kappa}{2} & 0 & -ig & 0 \\ 0 & -i\Delta_{da} - \frac{\kappa}{2} & 0 & ig \\ -ig & 0 & +i\Delta_{db} - \frac{\gamma}{2} + i2\Lambda|\bar{\beta}|^2 & i\Lambda(\bar{\beta}^2) \\ 0 & ig & -i\Lambda(\bar{\beta}^*)^2 & -i\Delta_{db} - \frac{\gamma}{2} - i2\Lambda|\bar{\beta}|^2 \end{pmatrix} \tag{B12}$$

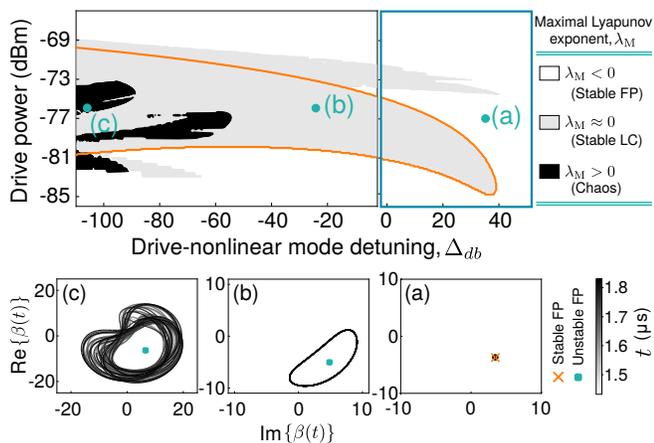Figure 5. **Calculated maximal Lyapunov exponent** λ_M **in Drive-Δ_{db} space.** The panel on the right framed in blue indicates the detuning range explored in Figs. 2, 3 of the main text. Solid orange curve indicates the linear stability boundary. In the white regions, $\lambda_M < 0$ is negative and the system is therefore stable. In the light gray regions, $\lambda_M \approx 0$, indicating a stable limit cycle. The dark regions are where $\lambda_M > 0$, and the system exhibits chaotic dynamics. Typical long-time dynamics projected in the nonlinear mode phase space are plotted in (a)-(c) corresponding to dynamics in the stable fixed point, stable limit cycle, and chaotic regimes respectively.

The stability of Eqs. (B11) is determined by the eigenvalues of the above Jacobian matrix, obtained by setting $\det \mathbf{J} = 0$; these are used to determine the stability boundaries obtained in the main text, and in Fig. 5 of the following appendix section.

Appendix C: Numerical phase diagram and Lyapunov stability

Regions in the classical phase diagram with no stable fixed points, Fig. 2, can give rise to a rich class of dynamics. Amongst various metrics to characterize such dynamics, we employ the standard technique of computing the maximal Lyapunov exponent λ_M, which describes the sensitivity of dynamical trajectories to small perturbations in the long-time limit. For details of the numerical approach tom computing λ_M, see SI[34].

The maximal Lyapunov exponent λ_M we calculate is plotted for Device A parameters in drive-Δ_{db} space in Fig. 5; the panel on the right framed in blue shows the region of drive-Δ_{db} space explored in Fig. 2. The blank regions indicate regions where $\lambda_M < 0$, indicating a stable fixed point; perturbations near this point decay over time, settling back towards the fixed point. This is visible in the projection of the steady-state dynamics onto the nonlinear mode phase space, plotted in Fig. 5 (a); in the long time limit the system has returned to the stable fixed point indicated by the orange cross. The gray regions indicate $\lambda_M \approx 0$, signifying a stable limit cycle attractor[58]. Steady-state dynamics here follow a stable phase space orbit, as shown in Fig. 5 (b), around a classically unstable fixed point (green square). The periodic orbits yield combs in the frequency domain, as observed in Fig. 5.

Finally, the dark regions indicate $\lambda_M > 0$. Here perturbations grow without bound over time, manifesting in dynamical chaos observed in numerical simulations of the classical system. The steady-state dynamics plotted in Fig. 5 (c) show how over time a single fixed orbit does not emerge and the system explores a large region of phase space in an irregular manner. The region framed in blue in the phase diagram describes the detuning range explored in the experiment, Figs. 2, 3 of the main text, where the system exhibits stable limit cycle dynamics,
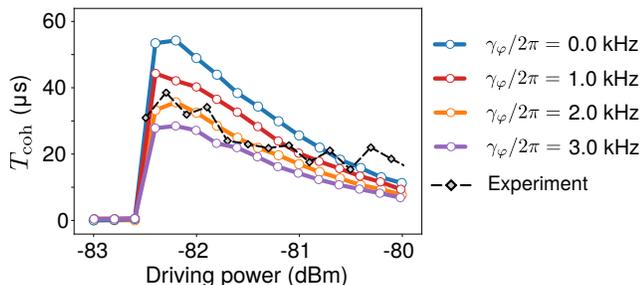
Figure 6. **Coherence times as a function of γ_φ.** Colored lines and points show numerically obtained T_{coh} values from the simulation of Eqs. (3) as a function of drive power, while dashed-diamonds indicate experimental values.

consistent with observations in the main text. However, for much more negative Δ_{db} it is possible to observe chaos with the same system. This indicates the potential of the two-mode system for controlled studies of chaos in the quantum regime; hints of this dynamics are seen in Fig. 4 of the main text, as well as for Device B (see SI).

Appendix D: Quantum simulations: comb coherence and estimating pure dephasing rate γ_φ

Simulating Eqs. (3) allows us to calculating the output coherence function, Eq. (2) defined in the main text; technical details of the simulations are included in Section III of the SI[34]. This enables us to extract the coherence time T_{coh}, as discussed in the main text. The only parameter required to simulate the SDEs that we are unable to directly measure is the pure dephasing rate γ_φ; the weak nonlinearity of the nonlinear mode prevents standard Ramsay measurement of the pure dephasing rate, and indirect methods based on cavity measurement are limited by the large disparity between the dephasing rate and the cavity linewidth κ. These difficulties are discussed in Section IV of the SI[34].

However, the coherence of frequency combs is affected by the known nonlinearity and the unknown pure dephasing rate; as a result, by simulating Eqs. (3) for various values of γ_φ and comparing with experimental observations, we can estimate γ_φ. In Fig. 6, we show the numerically obtained value of T_{coh} across the same cross-section of the phase diagram included in the main text, Fig. 2(b), for $\gamma_\varphi/(2\pi) \in [0.0, 1.0, 2.0, 3.0]$ kHz. Also shown is the experimental result. From these results we conclude that the pure dephasing rate may be well approximated to lie within $\gamma_\varphi/(2\pi) \in [1.0, 3.0]$ kHz. Furthermore, the best fit is found to be for $\gamma_\varphi/(2\pi) \simeq 2.0$ kHz.

Appendix E: Linearized Floquet Analysis of SDEs

The influence of quantum noise on system dynamics as described by the stochastic terms in Eqs. (3) is well understood when considering dynamics near a classically stable fixed point. Here one linearizes the system around the stable fixed point and studies weak fluctuations due to stochastic terms. However, in the frequency comb regime the system exhibits no classically stable fixed points, instead settling into a stable attractor describing a limit cycle. The study of linearized fluctuations around such stable attractors has gained much interest recently and can be performed by linearizing the dynamics around the periodic classical solution[36,44].

To begin, we rewrite the system of SDEs, Eqs. (A6), in the form below:

$$\frac{d\vec{\zeta}}{dt} = \vec{A}_{\mathrm{c}}(\vec{\zeta}) + \mathbf{B}_{\mathrm{st}}(\vec{\zeta}) \cdot \frac{d\vec{W}(t)}{dt} \qquad \text{(E1)}$$

where we have suppressed the dependence of $\vec{A}_{\mathrm{c}}, \mathbf{B}_{\mathrm{st}}$ on system parameters for notational convenience. In the frequency comb regime, the classical (noise-free) system admits the periodic solution $\vec{\zeta}_{\mathrm{c}}(t)$:

$$\frac{d\vec{\zeta}_{\mathrm{c}}}{dt} = \vec{A}_{\mathrm{c}}(\vec{\zeta}_{\mathrm{c}}) \qquad \text{(E2)}$$

For frequency combs with spacing Δ, $\vec{\zeta}_{\mathrm{c}}(t)$ is periodic with period $T = \frac{2\pi}{\Delta}$.

We can then consider fluctuations $\vec{z}(t)$ around this classical periodic solution:

$$\vec{\zeta}(t+\theta) = \vec{\zeta}_{\mathrm{c}}(t+\theta) + \vec{z}(t+\theta) \qquad \text{(E3)}$$

where we have introduced the additional phase parameter $\theta(t)$ which is not fixed by the classical dynamical equations of motion, and is therefore susceptible to perturbations due to noise (or other external stimuli)[36,44]. We are now interested in the linearized dynamics of the fluctuations $\vec{z}(t+\theta)$. Substituting the expansion, Eq. (E3), into the system of SDEs, Eq. (3), and retaining only terms linear in $\vec{z}(t)$, we find:

$$\frac{d\vec{z}}{dt} + \frac{d\vec{\zeta}_{\mathrm{c}}}{dt}\dot{\theta} = \mathbf{J}[\vec{\zeta}_{\mathrm{c}}(t)] \cdot \vec{z} + \mathbf{B}_{\mathrm{st}}[\vec{\zeta}_{\mathrm{c}}(t)] \cdot \frac{d\vec{W}}{dt} \qquad \text{(E4)}$$

where $\mathbf{J}[\vec{\zeta}_{\mathrm{c}}(t)]$ is the Jacobian matrix evaluated along the *periodic* classical solution, and is therefore a periodic matrix itself. Similarly $\mathbf{B}_{\mathrm{st}}[\vec{\zeta}_{\mathrm{c}}(t)]$ is the noise matrix also evaluated along the periodic classical solution. Finally, $\frac{d\vec{\zeta}_{\mathrm{c}}}{dt} \equiv \vec{v}$ is the velocity vector and is tangential to the limit cycle trajectory. This term clearly vanishes if $\vec{\zeta}_{\mathrm{c}}(t)$ is time *independent*, as in the case of a stable fixed point where $\vec{\zeta}_{\mathrm{c}}(t) \to \vec{Z}$ defined in Eq. (B9b); then the above equation simply describes the linearized dynamics of fluctuations around the fixed point, governed by a static Jacobian and driven by noise terms.

Here, however, the velocity term does not vanish and in addition to the dynamics of $\vec{z}(t)$, we are also interested in the evolution of the free phase $\theta(t)$ under the influence of stochastic terms. To solve for the dynamics

of a system governed by a time-periodic dynamical matrix, it proves useful to express the linearized fluctuations $\vec{z}(t)$ in terms of the Floquet eigenvectors defined by the *linearized* periodic system:

$$\frac{d\vec{z}}{dt} = \mathbf{J}[\vec{\zeta}_{\mathrm{c}}(t)] \cdot \vec{z} \qquad (\mathrm{E5})$$

Details of the Floquet eigensystem analysis are provided in the SI[34]; here for clarity we restrict our discussion to understanding how the main results can be used to analyze limit cycle phase diffusion. For convenience we define the periodic dynamical matrix $\mathbf{J}[\vec{\zeta}_{\mathrm{c}}(t)] \equiv \mathbf{J}(t)$ and the periodic noise matrix $\mathbf{B}_{\mathrm{st}}[\vec{\zeta}_{\mathrm{c}}(t)] \equiv \mathbf{B}_{\mathrm{st}}(t)$. The Floquet eigenvectors $\{\vec{p}_i(t), \vec{q}_i(t)\}$ for $i = 0, \ldots, N-1$ where N is the dimension of the system of ODEs ($N = 4$ for the present system), are periodic with the period of the stable classical limit cycle, T. They themselves satisfy the linear systems of equations:

$$\dot{\vec{p}}_i(t) = [\mathbf{J}(t) - \mu_i]\,\vec{p}_i(t) \qquad (\mathrm{E6a})$$

$$\dot{\vec{q}}_i^{\ddagger}(t) = \vec{q}_i^{\ddagger}(t)\,[\mu_i - \mathbf{J}(t)] \qquad (\mathrm{E6b})$$

The $\{\mu_i\}$ are Floquet exponents determined by the eigenvalues of the fundamental matrix of the Floquet system. For systems with a periodic stable attractor, at least one of the Floquet exponents, which we label μ_0 here, vanishes[58]. The corresponding Floquet eigenvector $\vec{p}_0(t)$ can be shown to be proportional to the tangential velocity vector $\vec{v}$ (see SI[34]). Finally, the Floquet eigenvectors satisfy the following orthogonality relation:

$$\vec{q}_j^{\ddagger}(t)\vec{p}_i(t) = \delta_{ij} \ \forall \ t \in [0, T] \qquad (\mathrm{E7})$$

To proceed, we expand the weak fluctuations around the stable limit cycle in terms of the Floquet eigenvectors:

$$\vec{z}(t) = \sum_{n=1}^{N-1} c_n(t)\vec{p}_n(t) \qquad (\mathrm{E8})$$

Note that the above expansion does not include the Floquet eigenvector $\vec{p}_0(t)$ corresponding to $\mu_0 = 0$, which as mentioned before is proportional to the tangent vector to the classical limit cycle[36]. Substituting the above expansion into the linearized set of SDEs, Eqs. (E4), we find:

$$\sum_{n=1}^{N-1} \left[\dot{c}_n(t)\vec{p}_n(t) + c_n(t)\dot{\vec{p}}_n(t) \right] + \vec{v}\dot{\theta}$$

$$= \mathbf{J}(t) \cdot \sum_{n=1}^{N-1} c_n(t)\vec{p}_n(t) + \mathbf{B}_{\mathrm{st}}(t) \cdot \frac{d\vec{W}}{dt} \qquad (\mathrm{E9})$$

where we now use Eq. (E6a) to eliminate $\mathbf{J}(t)\vec{p}_n(t)$; the terms corresponding to time derivatives of the right Floquet eigenvectors simply cancel, and we finally obtain:

$$\sum_{n=1}^{N-1} \dot{c}_n(t)\vec{p}_n(t) + \vec{v}\dot{\theta} = \sum_{n=1}^{N-1} \mu_n c_n(t)\vec{p}_n(t) + \mathbf{B}_{\mathrm{st}}(t) \cdot \frac{d\vec{W}}{dt}$$
$$(\mathrm{E10})$$

The remaining terms can be used to obtain equations of motion for the expansion coefficients. However, we are primarily interested in the diffusion of the phase variable $\theta(t)$. We can use the fact that $\vec{v}(t) \propto \vec{p}_0(t)$ to isolate the equation of motion for the phase variable: multiplying by the Floquet left eigenvector $\vec{q}_0^{\ddagger}(t)$ and using the orthogonality of the Floquet eigenvectors, the above system simplifies to:

$$\left(\vec{q}_0^{\ddagger}(t)\vec{v}(t) \right) \dot{\theta}(t) = \vec{q}_0^{\ddagger}(t) \left(\mathbf{B}_{\mathrm{st}}(t) \cdot \frac{d\vec{W}}{dt} \right) \qquad (\mathrm{E11})$$

For notational simplicity, we can normalize $\vec{q}_0(t)$ (and therefore $\vec{p}_0(t)$) such that $\vec{q}_0^{\ddagger}(t)\vec{v} = v_T$ where v_T is the root-mean-square velocity over the limit cycle period T, $v_T = \sqrt{\frac{1}{T} \int_0^T dt \, ||\vec{v}(t)||^2}$. Then, defining the time dependent noise projection of the noise vector in parenthesis onto $\vec{q}_0(t)$:

$$n(t) = \vec{q}_0^{\ddagger}(t) \left(\mathbf{B}_{\mathrm{st}}(t) \cdot \frac{d\vec{W}}{dt} \right) \qquad (\mathrm{E12})$$

we obtain the dynamical equation for $\theta(t)$:

$$v_T \dot{\theta}(t) = n(t) \qquad (\mathrm{E13})$$

which is the equation introduced in the main text. However, note that as introduced, the phase variable is a perturbation to the time t; it appears in the comb time evolution multiplied by the relevant frequency scale for frequency comb, namely the comb spacing Δ. We then have the equation of motion:

$$r_{\mathrm{eff}} \left[\Delta\dot{\theta}(t) \right] = n(t) \qquad (\mathrm{E14})$$

where we introduce the effective limit cycle radius r_{eff} via $v_T = r_{\mathrm{eff}}\Delta$ as in the main text. The simplified notation does require some caution; the noise term $n(t)$ is a stochastic term and solutions to the above equation must ultimately be determined by calculating moments of the phase variable. In particular, we can obtain the variance:

$$\Delta^2\langle\theta^2(t)\rangle = \frac{1}{r_{\mathrm{eff}}^2} \int_0^t \int_0^t d\tau \, d\tau' \, \langle n(\tau)n(\tau')\rangle \qquad (\mathrm{E15})$$

where we have set $\theta(0) = 0$, since only the relative phase is important. The double integral above simplifies once the noise correlation functions for white noise variables $\frac{d\vec{W}}{dt} = \vec{\xi}(t)$ are substituted. In particular since:

$$\langle\xi_i(\tau)\xi_j(\tau')\rangle = \delta_{ij}\delta(\tau - \tau') \qquad (\mathrm{E16})$$

we can write the variance of noise moments as:

$$\langle n(\tau)n(\tau')\rangle \equiv \langle n(\tau)^2\rangle\delta(\tau - \tau') \qquad (\mathrm{E17})$$

With the above definition, we can write the phase variance after a time equal to the period T as:

$$\Delta^2\langle\theta^2(T)\rangle = \frac{1}{r_{\mathrm{eff}}^2} \int_0^T d\tau\langle n(\tau)^2\rangle = T\left(\frac{\delta n}{r_{\mathrm{eff}}}\right)^2 \equiv 2\left(\frac{T}{T_{\mathrm{coh}}}\right)$$
$$(\mathrm{E18})$$

where we have introduced the average projected noise standard deviation as in the main text, $\delta n = \sqrt{\frac{1}{T} \int_0^T d\tau \, \langle n(\tau)^2 \rangle}$. The inset of the phase diagram in Fig. 3 of the main text plots T_{coh} as the limit cycle coherence time.

REFERENCES

[1] A. Blais, R.-S. Huang, A. Wallraff, S. M. Girvin, and R. J. Schoelkopf, "Cavity quantum electrodynamics for superconducting electrical circuits: An architecture for quantum computation," Phys. Rev. A **69**, 062320 (2004).

[2] S. M. Girvin, M. H. Devoret, and R. J. Schoelkopf, "Circuit QED and engineering charge-based superconducting qubits," Physica Scripta **T137**, 014012 (2009), publisher: IOP Publishing.

[3] S. M. Girvin, "Circuit QED: superconducting qubits coupled to microwave photons," in *Quantum Machines: Measurement and Control of Engineered Quantum Systems: Lecture Notes of the Les Houches Summer School: Volume 96, July 2011* (Oxford University Press, 2014) Chap. 3, p. 132.

[4] J. M. Martinis, M. H. Devoret, and J. Clarke, "Quantum Josephson junction circuits and the dawn of artificial atoms," Nature Physics **16**, 234–237 (2020), number: 3 Publisher: Nature Publishing Group.

[5] A. Blais, S. M. Girvin, and W. D. Oliver, "Quantum information processing and quantum optics with circuit quantum electrodynamics," Nature Physics **16**, 247–256 (2020).

[6] S. Haroche, M. Brune, and J. M. Raimond, "From cavity to circuit quantum electrodynamics," Nature Physics **16**, 243–246 (2020).

[7] R. Vijay, M. H. Devoret, and I. Siddiqi, "Invited review article: The josephson bifurcation amplifier," Review of Scientific Instruments **80**, 111101 (2009), https://doi.org/10.1063/1.3224703.

[8] T. Yamamoto, K. Inomata, M. Watanabe, K. Matsuba, T. Miyazaki, W. D. Oliver, Y. Nakamura, and J. S. Tsai, "Flux-driven josephson parametric amplifier," Applied Physics Letters **93**, 042510 (2008), https://doi.org/10.1063/1.2964182.

[9] M. A. Castellanos-Beltran and K. W. Lehnert, "Widely tunable parametric amplifier based on a superconducting quantum interference device array resonator," Applied Physics Letters **91**, 083509 (2007), https://doi.org/10.1063/1.2773988.

[10] J. Aumentado, "Superconducting parametric amplifiers: The state of the art in josephson parametric amplifiers," IEEE Microwave Magazine **21**, 45–59 (2020).

[11] A. Roy and M. Devoret, "Introduction to parametric amplification of quantum signals with Josephson circuits," Comptes Rendus Physique Quantum microwaves / Micro-ondes quantiques, **17**, 740–755 (2016).

[12] E. D. Walsh, D. K. Efetov, G.-H. Lee, M. Heuck, J. Crossno, T. A. Ohki, P. Kim, D. Englund, and K. C. Fong, "Graphene-based josephson-junction single-photon detector," Phys. Rev. Applied **8**, 024022 (2017).

[13] K. Inomata, Z. Lin, K. Koshino, W. D. Oliver, J.-S. Tsai, T. Yamamoto, and Y. Nakamura, "Single microwave-photon detector using an artificial ∧-type three-level system," Nature Communications **7**, 12303 (2016), number: 1 Publisher: Nature Publishing Group.

[14] A. Narla, S. Shankar, M. Hatridge, Z. Leghtas, K. M. Sliwa, E. Zalys-Geller, S. O. Mundhada, W. Pfaff, L. Frunzio, R. J. Schoelkopf, and M. H. Devoret, "Robust concurrent remote entanglement between two superconducting qubits," Phys. Rev. X **6**, 031036 (2016).

[15] A. Poudel, R. McDermott, and M. G. Vavilov, "Quantum efficiency of a microwave photon detector based on a current-biased josephson junction," Phys. Rev. B **86**, 174506 (2012).

[16] A. A. Clerk, K. W. Lehnert, P. Bertet, J. R. Petta, and Y. Nakamura, "Hybrid quantum systems with circuit quantum electrodynamics," Nature Physics **16**, 257–267 (2020).

[17] P. Del'Haye, A. Schliesser, O. Arcizet, T. Wilken, R. Holzwarth, and T. J. Kippenberg, "Optical frequency comb generation from a monolithic microresonator," Nature **450**, 1214–1217 (2007).

[18] P. Del'Haye, O. Arcizet, A. Schliesser, R. Holzwarth, and T. J. Kippenberg, "Full stabilization of a microresonator-based optical frequency comb," Phys. Rev. Lett. **101**, 053903 (2008).

[19] J. S. Levy, A. Gondarenko, M. A. Foster, A. C. Turner-Foster, A. L. Gaeta, and M. Lipson, "Cmos-compatible multiple-wavelength oscillator for on-chip optical interconnects," Nature Photonics **4**, 37–40 (2010).

[20] T. Herr, K. Hartinger, J. Riemensberger, C. Y. Wang, E. Gavartin, R. Holzwarth, M. L. Gorodetsky, and T. J. Kippenberg, "Universal formation dynamics and noise of Kerr-frequency combs in microresonators," Nature Photonics **6**, 480–487 (2012), number: 7 Publisher: Nature Publishing Group.

[21] T. Herr, V. Brasch, J. D. Jost, C. Y. Wang, N. M. Kondratiev, M. L. Gorodetsky, and T. J. Kippenberg, "Temporal solitons in optical microresonators," Nature Photonics **8**, 145 EP – (2013), article.

[22] T. J. Kippenberg, A. L. Gaeta, M. Lipson, and M. L. Gorodetsky, "Dissipative Kerr solitons in optical microresonators," Science **361** (2018), 10.1126/science.aan8083.

[23] A. L. Gaeta, M. Lipson, and T. J. Kippenberg, "Photonic-chip-based frequency combs," Nature Photonics **13**, 158–169 (2019).

[24] B. Stern, X. Ji, Y. Okawachi, A. L. Gaeta, and M. Lipson, "Battery-operated integrated frequency comb generator," Nature **562**, 401–405 (2018).

[25] M. Kues, C. Reimer, J. M. Lukens, W. J. Munro, A. M. Weiner, D. J. Moss, and R. Morandotti, "Quantum optical microcombs," Nature Photonics **13**, 170 (2019).

[26] R. P. Erickson, M. R. Vissers, M. Sandberg, S. R. Jefferts, and D. P. Pappas, "Frequency comb generation in superconducting resonators," Phys. Rev. Lett. **113**, 187002 (2014).

[27] N. R. Newbury and W. C. Swann, "Low-noise fiber-laser frequency combs (invited)," J. Opt. Soc. Am. B **24**, 1756–1770 (2007).

[28] S. Khan and H. E. Türeci, "Frequency combs in a lumped-element josephson-junction circuit," Phys. Rev. Lett. **120**, 153601 (2018).

[29] J. Koch, T. M. Yu, J. Gambetta, A. A. Houck, D. I. Schuster, J. Majer, A. Blais, M. H. Devoret, S. M. Girvin, and R. J. Schoelkopf, "Charge-insensitive qubit design derived from the cooper pair box," Phys. Rev. A **76**, 042319 (2007).

[30] I. Siddiqi, R. Vijay, F. Pierre, C. M. Wilson, M. Metcalfe, C. Rigetti, L. Frunzio, and M. H. Devoret, "RF-Driven Josephson Bifurcation Amplifier for Quantum Measurement," Physical Review Letters **93**, 207002 (2004), publisher: American Physical Society.

[31] J. Clarke and A. I. Braginski, *The SQUID Handbook* (Wiley-VCH, Weinheim, 2003).

[32] M. D. Hutchings, J. B. Hertzberg, Y. Liu, N. T. Bronn, G. A. Keefe, M. Brink, J. M. Chow, and B. L. T. Plourde, "Tunable Superconducting Qubits with Flux-Independent Coherence," Physical Review Applied **8**, 044003 (2017).

[33] H. Paik, D. I. Schuster, L. S. Bishop, G. Kirchmair, G. Catelani, A. P. Sears, B. R. Johnson, M. J. Reagor, L. Frunzio, L. I. Glazman, S. M. Girvin, M. H. Devoret, and R. J. Schoelkopf, "Observation of high coherence in josephson junction qubits measured in a three-dimensional circuit qed architecture," Phys. Rev. Lett. **107**, 240501 (2011).

[34] "See supplementary information available at xxx for details of classical linearized and full numerical stability analysis, experimental details of kerr nonlinearity measurement and supplementary phase diagrams, and quantum description of comb phase diffusion." .

[35] M. J. Ablowitz, B. Ilan, and S. T. Cundiff, "Noise-induced linewidth in frequency combs," Optics Letters **31**, 1875–1877 (2006), publisher: Optical Society of America.

[36] C. Navarrete-Benlloch, T. Weiss, S. Walter, and G. J. de Valcarcel, "General Linearized Theory of Quantum Fluctuations around Arbitrary Limit Cycles," Physical Review Letters **119**, 133601 (2017).

[37] N. Coluccelli, M. Cassinerio, A. Gambetta, P. Laporta, and G. Galzerano, "Frequency-noise measurements of optical frequency combs by multiple fringe-side discriminator," Scientific Reports **5**, 1–10 (2015), number: 1 Publisher: Nature Publishing Group.

[38] M. P. da Silva, D. Bozyigit, A. Wallraff, and A. Blais, "Schemes for the observation of photon correlation functions in circuit QED with linear detectors," Physical Review A **82**, 043804 (2010).

[39] H. J. Carmichael, *Statistical Methods in Quantum Optics 1 - Master Equations and Fokker-Planck Equations | Howard J. Carmichael | Springer* (2002).

[40] P. D. Drummond and C. W. Gardiner, "Generalised P-representations in quantum optics," Journal of Physics A: Mathematical and General **13**, 2353–2368 (1980).

[41] O. Maillet, F. Vavrek, A. D. Fefferman, O. Bourgeois, and E. Collin, "Classical decoherence in a nanomechanical resonator," New Journal of Physics **18**, 073022 (2016).

[42] M. Aspelmeyer, T. J. Kippenberg, and F. Marquardt, "Cavity optomechanics," Reviews of Modern Physics **86**, 1391–1452 (2014).

[43] C. Eichler and A. Wallraff, "Controlling the dynamic range of a josephson parametric amplifier," EPJ Quantum Technology **1**, 2 (2014).

[44] A. Demir, A. Mehrotra, and J. Roychowdhury, "Phase noise in oscillators: a unifying theory and numerical methods for characterization," IEEE Transactions on Circuits and Systems I: Fundamental Theory and Applications **47**, 655–674 (2000), conference Name: IEEE Transactions on Circuits and Systems I: Fundamental Theory and Applications.

[45] P. D. Drummond and P. Deuar, "Quantum dynamics with stochastic gauge simulations," J. Opt. B: Quantum Semiclass. Opt. **5**, S281–S289 (2003).

[46] C. W. Gardiner and M. J. Collett, "Input and output in damped quantum systems: Quantum stochastic differential equations and the master equation," Physical Review A **31**, 3761–3774 (1985).

[47] J. Bylander, S. Gustavsson, F. Yan, F. Yoshihara, K. Harrabi, G. Fitch, D. G. Cory, Y. Nakamura, J.-S. Tsai, and W. D. Oliver, "Noise spectroscopy through dynamical decoupling with a superconducting flux qubit," Nature Physics **7**, 565–570 (2011).

[48] F. Yan, S. Gustavsson, J. Bylander, X. Jin, F. Yoshihara, D. G. Cory, Y. Nakamura, T. P. Orlando, and W. D. Oliver, "Rotating-frame relaxation as a noise spectrum analyser of a superconducting qubit undergoing driven evolution," Nature Communications **4**, 2337 (2013).

[49] G. Andersson, B. Suri, L. Guo, T. Aref, and P. Delsing, "Non-exponential decay of a giant artificial atom," Nature Physics **15**, 1123–1127 (2019).

[50] A. Gilchrist, C. W. Gardiner, and P. D. Drummond, "Positive p representation: Application and validity," Phys. Rev. A **55**, 3014–3032 (1997).

[51] N. E. Frattini, U. Vool, S. Shankar, A. Narla, K. M. Sliwa, and M. H. Devoret, "3-wave mixing Josephson dipole element," Applied Physics Letters **110**, 222603 (2017), publisher: American Institute of Physics.

[52] A. Essig, Q. Ficheux, T. Peronnin, N. Cottet, R. Lescanne, A. Sarlette, P. Rouchon, Z. Leghtas, and B. Huard, "Multiplexed photon number measurement," arXiv:2001.03217 [cond-mat, physics:quant-ph] (2020), arXiv: 2001.03217.

[53] K. M. Sliwa, M. Hatridge, A. Narla, S. Shankar, L. Frunzio, R. J. Schoelkopf, and M. H. Devoret, "Reconfigurable josephson circulator/directional amplifier," Phys. Rev. X **5**, 041020 (2015).

[54] F. Lecocq, L. Ranzani, G. A. Peterson, K. Cicak, R. W. Simmonds, J. D. Teufel, and J. Aumentado, "Nonreciprocal microwave signal processing with a field-programmable josephson amplifier," Phys. Rev. Applied **7**, 024028 (2017).

[55] A. Metelmann and H. E. Türeci, "Nonreciprocal signal routing in an active quantum network," Phys. Rev. A **97**, 043833 (2018).

[56] V. V. Sivak, N. E. Frattini, V. R. Joshi, A. Lingenfelter, S. Shankar, and M. H. Devoret, "Kerr-free three-wave mixing in superconducting quantum circuits," Phys. Rev. Applied **11**, 054060 (2019).

[57] C. Gardiner, *Stochastic Methods: A Handbook for the Natural and Social Sciences*, Springer Series in Synergetics (Springer Berlin Heidelberg, 2009).

[58] H. Haken, "At least one Lyapunov exponent vanishes if the trajectory of an attractor does not contain a fixed point," Physics Letters A **94**, 71–72 (1983).